Century-long cooling trend in subpolar North Atlantic forced by atmosphere: an alternative explanation

Laifang Li[1,4,5] · M. Susan Lozier[2] · Feili Li[2,3]

Abstract

A well-known exception to rising sea surface temperatures (SST) across the globe is the subpolar North Atlantic, where SST has been declining at a rate of 0.39 ($\pm$ 0.23) K century^{-1} during the 1900–2017 period. This cold blob has been hypothesized to result from a slowdown of the Atlantic Meridional Overturning Circulation (AMOC). Here, observation-based evidence is used to suggest that local atmospheric forcing can also contribute to the century-long cooling trend. Specifically, a 100-year SST trend simulated by an idealized ocean model forced by historical atmospheric forcing over the cold blob region matches 92% ($\pm$ 77%) of the observed cooling trend. The data-driven simulations suggest that 54% ($\pm$ 77%) of the observed cooling trend is the direct result of increased heat loss from the ocean induced by the overlying atmosphere, while the remaining 38% is due to strengthened local convection. An analysis of surface wind eddy kinetic energy suggests that the atmosphere-induced cooling may be linked to a northward migration of the jet stream, which exposes the subpolar North Atlantic to intensified storminess.

1 Introduction

In response to the input of anthropogenic greenhouse gases, sea surface temperature (SST) has been increasing almost everywhere since the 1900s (Levitus et al. 2001; Hansen et al. 2005; IPCC 2013). A notable exception to this global warming pattern is a 'cold blob' (also known as a 'warming hole')[1] situated over the subpolar North Atlantic (Drijfhout

✉ Laifang Li
lfl5240@psu.edu

1 Department of Meteorology and Atmospheric Science, Pennsylvania State University, University Park, PA 16802, USA

2 School of Earth and Atmospheric Sciences, Georgia Institute of Technology, Atlanta, GA 30332, USA

3 Present Address: State Key Laboratory of Marine Environmental Science and College of Ocean and Earth Sciences, Xiamen University, Xiamen, Fujian, China

4 Institute of Computational and Data Sciences, Pennsylvania State University, University Park, PA 16802, USA

5 Earth and Environmental Systems Institute, Pennsylvania State University, University Park, PA 16802, USA

et al. 2012; Rahmstorf et al. 2015), where SST has been decreasing over the past century (Fig. 1a). The observed cooling is most significant over the central portion of the eastern subpolar gyre, most notably the Irminger Sea (−0.39 [$\pm$ 0.23][2] K century^{-1}) (Fig. 1a). In addition, the SSTA cooling trend is more significant during the cold season (−0.44 [$\pm$ 0.26] K century^{-1} for December–January–February–March) than during the warm season (−0.31 [$\pm$ 0.32] K century^{-1} for July–August–September–October) (Fig. 1b).

Previous studies have offered this regional cooling as evidence of a slowdown of the Atlantic Meridional Overturning Circulation (AMOC), whereby there is a reduction in the heat transport to the subpolar North Atlantic (Rahmstorf et al. 2015; Sevellec et al. 2017; Sgubin et al. 2017; Caesar et al. 2018). This AMOC slowdown hypothesis is supported by climate model studies, however, these studies

---

[1] We acknowledge that the term 'warming hole' is more commonly used to describe the absence of warming in the subpolar North Atlantic in response to anthropogenic greenhouse gases. However, based on our analysis of multiple SSTA datasets, we opt to use 'cold blob' as it more accurately reflects the statistically significant SSTA cooling trend observed over the subpolar North Atlantic.

[2] The value in brackets represents the 95% confidence interval of the SSTA centennial trend based on linear regression coefficients.

a Global SSTA trend (1900-2017)

b
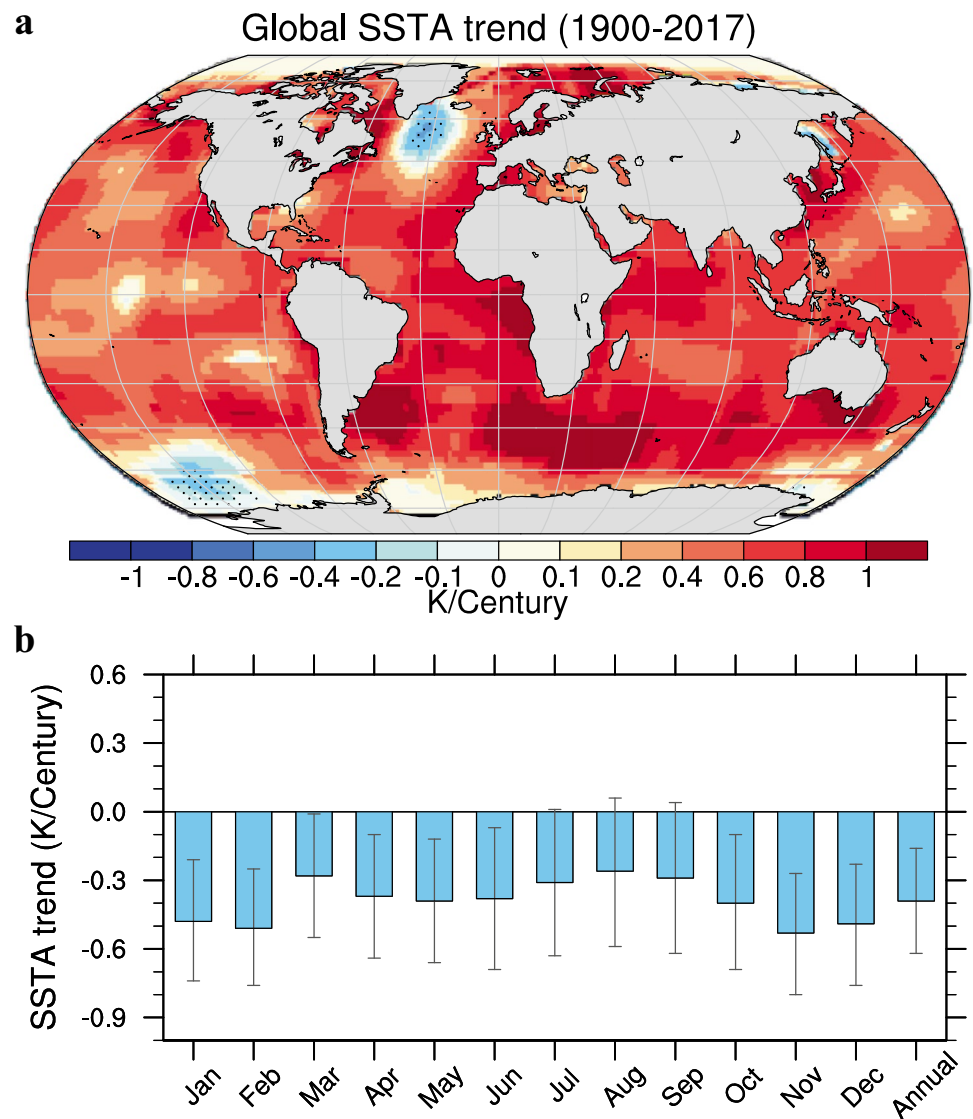
are not consistent in terms of the spatial pattern and timing of the cold blob in response to an AMOC slowdown (Drijfhout et al. 2012; Gervais et al. 2018; Menary and Wood 2018). Given these inconsistencies and the lack of direct observational evidence of an AMOC slowdown over the past century (Fu et al. 2020; Worthington et al. 2021), the forcing mechanism responsible for the cold blob remains an open question.

In addition to the AMOC influence, SST in the subpolar North Atlantic is impacted by a host of local processes involving both the atmosphere and the ocean circulation (Clement et al. 2015; Foukal and Lozier 2018; Hu and Fedorov 2020; Keil et al. 2020; Wills et al. 2019). In particular, recent observations in the Irminger Sea have attributed the record-low SSTs in the winters of 2014/2015 and 2015/2016 to exceptionally strong heat loss from the ocean to the atmosphere (de Jong and de Steur 2016; Josey et al.

2018, 2019). The heat loss is further attributable to intensified local winds associated with a North Atlantic Oscillation-like atmospheric circulation pattern during those winters (Josey et al. 2019). Examinations of century-long atmospheric observations and climate simulations have shown substantial changes in the atmospheric circulation over the subpolar North Atlantic in the past century. These changes are manifested by a northward movement of the jet stream and increased storminess (e.g., Woollings et al. 2012; Feser et al. 2015; Chang and Yan 2016). While studies have emphasized the role of oceanic heat transport in causing these observed changes in the atmospheric circulation (e.g., Woollings et al. 2012; Gulev et al. 2013; Gervais et al. 2019), reciprocity—whereby the SSTA is impacted by atmospheric forcing— is expected since air-sea heat fluxes will respond to altered surface meteorological conditions (Ma et al. 2020).

The extent to which these long-term changes in the atmosphere can account for the observed cold blob is the focus of this study. Essentially, we are asking whether the observed SST variability can be at least partially attributed to local processes. For our investigation, we choose an idealized one-dimensional (1-D) ocean heat balance model rather than fully coupled global climate models (GCMs) because the uncertainties in simulating the location and spatial pattern of the cold blob in these GCMs (Menary and Wood 2018) hampers their application to our study of the cold blob forcing mechanism. In addition, SSTA variability in GCMs results from both atmospheric forcing and ocean dynamics, and their separate impacts—which we want to know for our study—cannot be easily isolated. As detailed in Sect. 2.1, the observationally constrained model that we have built allows us to isolate the SSTA cooling caused exclusively by observed changes in the local atmospheric forcing during the past century. With this model, we are able to address the extent to which local atmospheric processes can explain the observed cold blob.

2 Methods

In this section, we first derive a 1-D ocean heat balance model that isolates the SST response to local atmospheric forcing. We then outline the observational datasets used to diagnose the SSTA trend and derive the parameters of the model.

2.1 Idealized 1-D two-compartment ocean heat balance model

In this study, an idealized 1-D two-compartment model is applied. The model conceptualizes the ocean as two thermodynamically-active layers: the surface mixed layer and the subsurface thermocline. In order to isolate the SSTA trend due to local atmospheric forcing, the horizontal oceanic heat flux is purposely ignored in our local heat balance, thus simplifying the model to 1-D. We acknowledge that this 1-D model cannot reproduce the complicated ocean dynamics in the subpolar North Atlantic (e.g. Buckley and Marshall 2016; Zhang et al. 2019), but, as stated above, our goal is to ascertain the extent to which 1-D dynamics can explain the observed cold blob. With this model choice, a mismatch between the modelled SSTA trend and that observed will reflect the role of horizontal oceanic heat transport, whether due to the AMOC (Rahmstorf et al. 2015; Sevellec et al. 2017), subpolar gyre circulation (Keil et al. 2020) and/or mesoscale eddies.

In this model, heat flux across the air-sea interface directly forces temperature variability in the mixed layer and is the only external heat source for the two layers.

Heat exchange between the two layers is accomplished via thermal coupling processes (i.e., diffusion, mixing, and entrainment/detrainment) (Gregory 2000; Held et al. 2010; Gupta and Marshall 2018). With these assumptions and simplifications, heat conservation in the two layers is modeled as:

$$\rho C_p h_1 \frac{\partial T_1}{\partial t} = Q_{net} + \rho C_p q_1 (T_2 - T_1), \tag{1}$$

$$\rho C_p h_2 \frac{\partial T_2}{\partial t} = \rho C_p q_2 (T_1 - T_2), \tag{2}$$

where $\rho = 1024$ Kg m^{-3} is the reference density and $C_p = 3850$ J Kg^{-1} K^{-1} is the specific heat of sea water. h_1 and h_2 (unit: m) are the mixed layer depth (MLD) and the thickness of the subsurface layer, respectively. T_1 is mixed layer temperature (equivalent to SST in this model configuration), and T_2 is subsurface temperature. Q_{net} (unit: Wm^{-2}) is net surface heat flux, which is the sum of net shortwave radiation (Q_{sw}), net longwave radiation (Q_{lw}), sensible heat flux (Q_{sh}) and latent heat flux (Q_{lh}). Heat flux is positive when the flux is into the ocean. Both q_1 and q_2 are heat exchange rates (unit: ms^{-1}) between the surface and subsurface, which reflect the strength of surface/subsurface thermal coupling (Held et al. 2010). $q_1 = q_{diff} + w_{ent}$ is the sum of diffusion/mixing (q_{diff}) and the entrainment velocity (w_{ent}), with the latter dominating in the subpolar North Atlantic during the convection season (Alexander and Deser 1995; Deser et al. 2003; Hanawa and Sugimoto 2004). $q_2 = q_{diff} + w_{det}$ is quantified as the sum of diffusion/mixing (q_{diff}) and the detrainment velocity (w_{det}). In the analysis, entrainment/detrainment velocity are calculated based on the rate of change of the MLD:

$$w_{ent} = \frac{dh_1}{dt} \Gamma \left(\frac{dh_1}{dt} \right), \tag{3}$$

$$w_{det} = \frac{dh_1}{dt} \Gamma \left(-\frac{dh_1}{dt} \right). \tag{4}$$

Here, $\Gamma(x) = \begin{cases} x, & x > 0 \\ 0, & x \leq 0 \end{cases}$ is a heaviside function. Climatologically, the MLD over the cold blob deepens in the winter months (November–December–January–February) and subsurface cold water is entrained into the mixed layer (blue bars in Fig. 2a). The entrainment process decreases surface temperature, but has no impact on the subsurface layer. In contrast, the MLD shoals from late spring until summer (April–May–June–July; red bars in Fig. 2a). The stratification of the surface layer detrains warm water into the subsurface, and thus warms the subsurface but does not change the mixed layer temperature. Due to the

Fig. 2 a Climatology of entrainment (blue bars) and detrainment velocity (red bars) calculated from Eqs. 3–4. The error bars represent the standard error of the climatology estimated using the 1950–2009 samples. b and c Are, respectively, the time series of the wintertime entrainment and the summertime detrainment velocity throughout 1950–2009. The thick solid lines are linear trends and the corresponding dashed lines are the 95% uncertainty range of the liner trends derived from the regression analysis
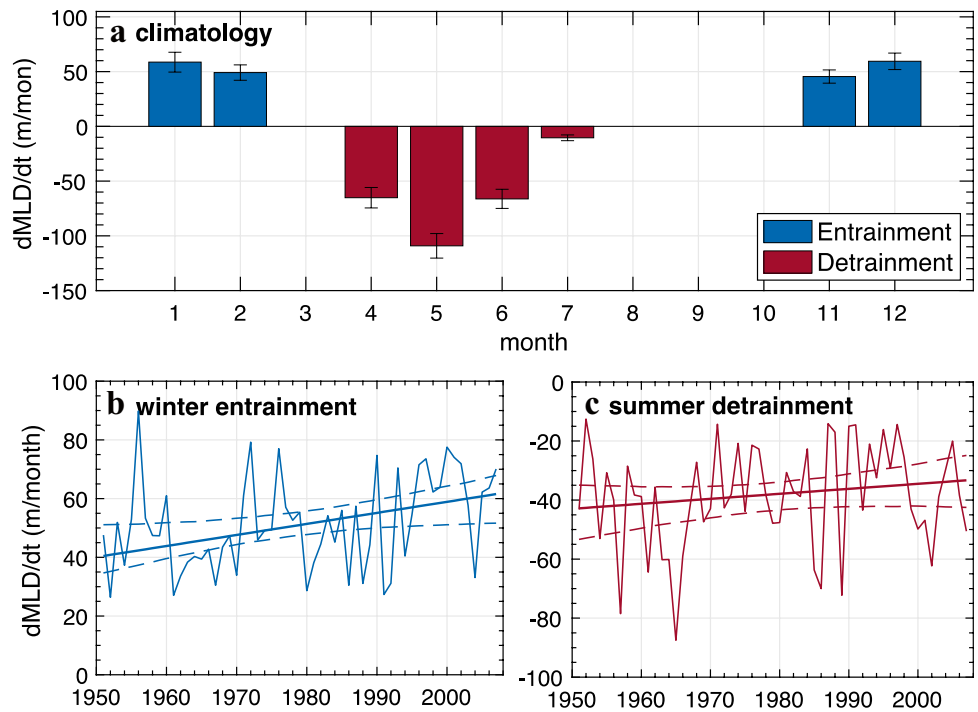
seasonal dependence of detrainment and entrainment processes, $q_1 \neq q_2$ and surface–subsurface heat exchange should be parameterized separately.

To quantify the evolution of temperature anomalies in the two compartments, the monthly climatology for temperature and for the forcing terms are removed from Eqs. (1) and (2):

$$\rho C_p h_1 \frac{\partial T_1'}{\partial t} = Q_{net}' + \rho C_p \left[q_1 (T_2 - T_1) \right]', \tag{5}$$

$$\rho C_p h_2 \frac{\partial T_2'}{\partial t} = \rho C_p \left[q_2 (T_1 - T_2) \right]'. \tag{6}$$

Here, the prime is the deviation from the monthly climatology. Equation (5) suggests that the local atmosphere can *directly* force SSTA variability through the surface heat flux anomaly and *indirectly* through the changes surface/subsurface heat exchange, assuming that horizontal heat divergence is minimal. Ignoring the higher order terms,[3] Eqs. (5) and (6) are linearized as:

$$\rho C_p h_1 \frac{\partial T_1'}{\partial t} = Q_{net}' + \rho C_p \overline{q}_1 (T_2' - T_1') + \rho C_p q_1' \left(\overline{T_2} - \overline{T_1} \right), \tag{7}$$

$$\rho C_p h_2 \frac{\partial T_2'}{\partial t} = \rho C_p \overline{q}_2 (T_1' - T_2') + \rho C_p q_2' \left(\overline{T_1} - \overline{T_2} \right). \tag{8}$$

Further, Q_{net}' is separated into two terms: $Q_{net}' = -\alpha T_1' + Q_{atmo}'$. The first term on the right-hand side, which quantifies the dependence of surface heat flux on the existing SSTA (Frankignoul et al. 1998; Hausmann et al. 2017; Li et al. 2020), acts as a damping mechanism on SSTA. Here, α is the SSTA damping coefficient (unit: W m^{-2} K^{-1}). The second term (Q_{atmo}') reflects the atmospheric thermal forcing on SSTA, as it is the portion of Q_{net}' independent of SSTA but dependent on atmospheric processes (i.e., air temperature, surface humidity and surface wind). Detailed derivations of α and Q_{atmo}' are formulated in "Appendix" (Eqs. A9–A13). Due to the short persistence of atmospheric forcing (7–10 days; Feldstein 2000) and its observed long-term trend (Fig. 3), Q_{atmo}' can be approximated by $Q_{atmo}' = N(0, \sigma^2) + Q_{atmo\_trend}'$. Following previous studies, the randomness of atmospheric forcing is represented by a normally distributed white-noise function with variance σ^2 (Hasselmann 1976; Frankignoul et al. 1998; Schneider and Cornuelle 2005; Di Lorenzo and Ohman 2013; Chen et al. 2016; Li et al. 2020). Detailed quantification of σ^2 is formulated in Li et al. (2020). Q_{atmo_trend}' is the centennial trend in Q_{atmo}' (see details in the Sect. 2.3). In addition, since

---

[3] The higher order term $q_1' (T_2' - T_1')$ is roughly one order of magnitude smaller than $\overline{q}_1 (T_2' - T_1')$ in that $\left| q_1' \right| \sim 0.28 \overline{q}_1$ according to Fig. 2b.
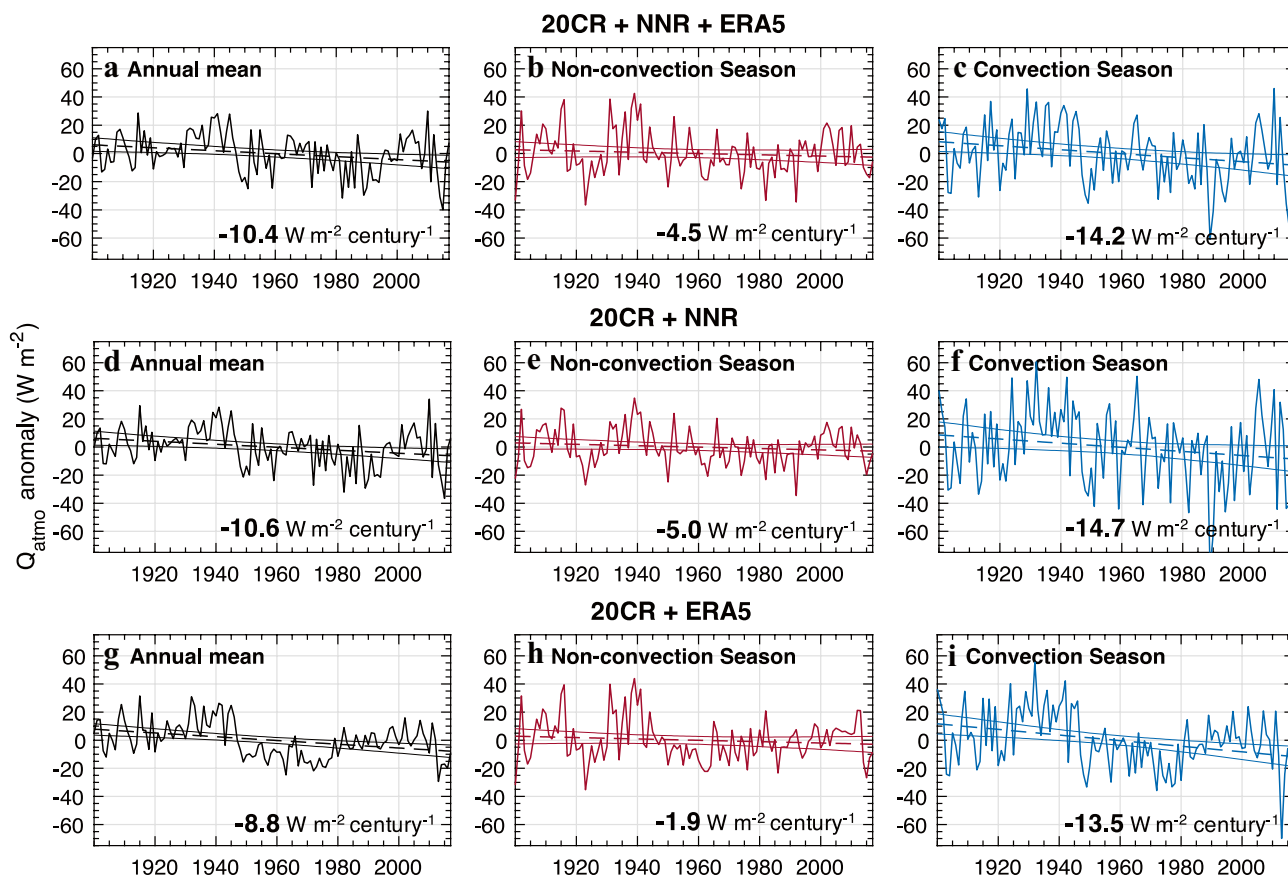
Fig. 3 Q'_{atmo} calculated over the cold blob region (solid lines) and its linear trend (thick dashed lines) during 1900–2017. The plots in the left, middle, and right columns show, respectively, annual mean Q'_{atmo} (**a**, **d**, **g**), average Q'_{atmo} during the non-convection season (JASO; **b**, **e**, **h**), and average Q'_{atmo} during the convection season (DJFM; **c**, **f**, **i**). The upper panels (**a**–**c**) are the calculation based on the combination of the 20CR, NNR, and ERA5 reanalysis products; the middle panels (**d**–**f**) are based on the combination of 20 CR and NNR; and the lower panels (**g**–**i**) are the combination of 20CR and ERA5. In each plot, the thin solid lines are the 95% uncertainty range of the linear trend. Detailed calculation of Q'_{atmo} is formulated in "Appendix"

no significant change in q_2 has been observed[4] (Fig. 2c), the term involving q'_2 is assumed to be zero.

With these simplifications, the two-compartment model describing temperature anomalies in the cold blob is formulated as:

$$\rho C_p h_1 \frac{\partial T'_1}{\partial t} = \underbrace{-\alpha T'}_{1} + \underbrace{N(0, \sigma^2)}_{2} + \underbrace{Q'_{atmo_{trend}}}_{} + \underbrace{\rho C_p \overline{q}_1 (T'_2 - T'_1)}_{3} + \underbrace{\rho C_p q'_1 \left(\overline{T_2} - \overline{T_1}\right)}_{4},$$

$$\rho C_p h_2 \frac{\partial T'_2}{\partial t} = \rho C_p \overline{q}_2 (T'_1 - T'_2). \tag{10}$$

All parameters (h_1, h_2, α, $\overline{q}_1$ and $\overline{q}_2$) in the two-compartment model are derived using observation-based data-sets and are averages over the cold blob region (outlined in Fig. 1a). Thus, the model parameters are observationally constrained and unique for the cold blob. Specifically, h_1 is the monthly climatology of the MLD derived from T/S profiles over the cold blob region, h_2 is set to 1000 m, $\alpha = 26.26\ \text{Wm}^{-2}\ \text{K}^{-1}$ is the SSTA damping coefficient in the

---

[4] According to our analysis, the linear trend in summertime detrainment is 14 m month^{-1} century^{-1}, but the p-value is 0.28 (not statistically significant). It is noteworthy that the starting point to calculate MLD is set to 1950 due to limited observations over the subpolar North Atlantic prior to the 1950s. EN4.2.1 uses climatology to fill in missing observations, which potentially underestimates the observed trend in MLD. We thus extrapolate the trend line based on the 1950–2009 period when increased data samples are available.

region.[5] $\overline{q}_1$ and $\overline{q}_2$ are derived based on the monthly variation of MLD (Fig. 2a).

Term 1 in Eq. (9) represents the forcing due to atmospheric white noise. Term 2 is the long-term trend in atmospheric forcing. Term 3 is the temperature adjustment which represents the change of ocean stratification ($T'_2 - T'_1$) throughout the simulation. Term 4 is the SSTA variation due to changes in surface–subsurface coupling strength (q'_1), which shows a significant increasing trend in the past century, evidenced by the intensification of entrainment (Fig. 2b; the linear trend is 30 m month^{-1} century^{-1} with a p value of 0.003, suggesting the trend is statistically significant).

We perform the four simulations with each of the four terms in Eq. (9) added sequentially. In the first two simulations, no heat transfer between the surface and subsurface (terms 3 and 4 in Eq. 9) is considered. Thus, the two-compartment model is equivalent to a one-compartment slab ocean model. All four simulations are run for 100 years with monthly temporal resolution. We also set T'_1 and T'_2 to 0 at the start of each simulation. Each simulation consists of 1000 runs to quantify the uncertainty range of the centennial SST trend. In all four simulations, the seasonal cycle of h_1 (mixed layer depth) is fixed throughout the 100-year period (i.e., h_1 changes with month but does not evolve interannually), even though wintertime h_1 is expected to deepen with surface cooling by the atmosphere (Figs. 2b and 3). We performed simulations which allow h_1 to deepen at an observed rate, and found that this inclusion changed the total simulated SSTA trends by less than 1% (not shown).

2.2 PWP mixed layer model

q'_1 changes in the 2-compartment model are quantified by an MLD deepening rate (i.e., convection) during the convection season (term 4 in Eq. 9). In the subpolar North Atlantic, MLD deepens due to various factors including atmospheric forcing, ocean advection, and eddies (Alexander et al. 2000; Pickart et al. 2003; Carton et al. 2008; Våge et al. 2008; Fröb et al. 2016; de Jong and de Steur 2016). In order to quantify ocean convection changes due to local atmospheric forcing alone, we apply the Price-Weller-Pinkel (PWP) mixed layer model (Price et al. 1986). The PWP model is a one-dimensional model forced by buoyancy (heat and freshwater

fluxes) and momentum (wind stress) fluxes across the air–sea interface. In the model, convection (i.e., mixing) takes place when the density profile becomes unstable due to (1) changes in the surface heat or freshwater flux that result in a negative buoyancy flux for the existing mixed layer or (2) the flow at the bottom of the mixed layer exceeds the shear instability criteria ($R_i < 0.65$) (Price et al. 1986). The PWP model simulation is initialized with the climatological August (i.e., late summer) temperature/salinity (T/S) profile averaged over the cold blob region outlined in Fig. 1a. The forcing fields are the 6-hourly surface heat fluxes, freshwater fluxes (evaporation – precipitation rate), and wind stress from the twentieth Century Reanalysis (Compo et al. 2011). Because we are interested in isolating the change in convection/mixing due to surface atmospheric forcing, the T/S profile is not reinitialized during the simulations to match the observed T/S profiles during 1900–2017 (Holliday et al. 2015, 2020).

From the PWP model simulations, an incidence of convection/mixing is counted when an assigned value of surface turbulent heat flux leads the onset of static or shear instability. At that point, the probability of convection is calculated corresponding to the given surface heat flux. We then fit an empirical function to describe the relationship between probability of convection and surface turbulent heat flux in the form of:

$$P\big(Convection|Q_{turb}\big) = 1.03 exp\left(-\frac{22.87}{Q_{turb}}\right). \tag{11}$$

This empirical function is applied in the fourth simulation where changes in the heat exchange rate are considered (term 4 in Eq. 9). Specifically, we first calculate the heat flux anomaly (Q'_{turb}, where $Q'_{turb} = -\alpha T' + N(0, \sigma^2) + Q'_{atmo\_trend}$) from the two-compartment model. We then insert $Q_{turb} = Q'_{turb} + \overline{Q_{turb}}$ into Eq. (11) to calculate the convection probability for that heat flux anomaly. This probability is converted to entrainment velocity anomalies (w'_{ent}) by assuming a linear relationship, i.e., a 10% increase in convection probability is equivalent to a 10% increase in entrainment velocity.

2.3 Datasets

The data analyzed in this study are from observation-based sources. The SST records are compiled using three century-long datasets: Extended Reconstructed SST (ERSST) version 4 (ERSST V4; Huang et al. 2014; Liu et al. 2014), Hadley Center Sea Ice and Sea Surface Temperature (HadISST; Rayner et al. 2003), and Kaplan SST (Kaplan et al. 1998). SSTs from the three datasets are first interpolated to 2×2 grid cells using bilinear regression methods. The monthly climatology of SST is removed from the original data to

---

[5] This damping coefficient (α) is derived using the combination of three reanalysis data products: 20CR, NNR and ERA5 (see Sect. 2.3). We have also assessed α using the combination of 20CR and NNR as well as the combination of 20CR and ERA5. The resultant α value for the two combinations is 24.75 Wm^{-2} K^{-1} and 27.11 Wm^{-2} K^{-1}, respectively.

calculate monthly SSTAs. The centennial SSTA trends calculated from each of these three datasets are consistent in terms of the location of the cold blob, i.e., the cooling trend is mainly located in the eastern subpolar gyre, particularly so in the Irminger Sea (Fig. 4). Rather than favoring one dataset over the others, we use the average SSTA from the three datasets as the best estimate of observed SSTA for our period of study.

The SSTA time series representing the cold blob is the areal-averaged SSTA where a significant cooling trend ($\alpha < 0.05$) in annual mean SSTA is present during the 1900–2017 period (stippled grid cells in Fig. 1a). To estimate the seasonal variability of the cold blob trend, we calculate the SSTA trend for each month using linear regression. The uncertainty range of the linear trend (error bars in Fig. 1b) is defined as the 95% confidence interval of the trend line, derived using linear regression. The cold blob SSTA time series (1900–2017) are shown in Fig. 5 for the annual mean, non-convection season and convection season. As expected, the SSTA time series exhibit multidecadal variability due to the expression of the Atlantic Multidecadal Variability (AMV) on the subpolar North Atlantic (Schlesinger and Ramankutty 1994; Kerr 2000; Wills et al., 2019; Li et al., 2020). Also as expected, the presence of the low frequency multidecadal variation complicates the detection of the SSTA linear trend. Specifically, the trend in the non-convection season becomes insignificant with this natural variation (Fig. 5b). However, the trend of annual mean SSTA and that during the convection-season remain statistically significant at a level of $\alpha = 0.05$ (Fig. 5a and c).

MLD (h_1) is derived from the EN4.2.1 gridded monthly temperature and salinity fields (Good et al. 2013) using the potential density criteria of $\Delta\rho = 0.125 \, \text{kgm}^{-3}$, i.e. MLD is the depth where potential density increases by 0.125 kg m^{-3} over the surface (5 m) value (Monterey and Levitus 1997; de Boyer Montegut et al. 2004).

Surface heat fluxes are from the twentieth Century Reanalysis (20CR) version 2 (Compo et al. 2011) for 1870–2012; NCEP/NCAR reanalysis (NNR; Kalnay et al. 1996) for 1948–2017; and ERA5 reanalysis (Hersbach et al. 2020) for 1950–2017. We averaged the three datasets during their overlapping period to generate a best estimate of net surface heat flux (Q_{net}) for the past century. Similarly, we also estimated Q_{net} using the combination of 20CR and NNR, as well as 20CR and ERA5. In total, we have three estimates of Q_{net}, which allow us to quantify the uncertainties of the model parameters in Eq. (9) due to the choice of reanalysis products. Q_{net} is calculated as $Q_{net} = Q_{sw} - Q_{lw} - Q_{sh} - Q_{lh}$, where Q_{sw} is net downward shortwave radiation, Q_{lw} is net upward long wave radiation, and Q_{sh} and Q_{lh} are, respectively, sensible and latent heat flux from the ocean to the atmosphere. Q_{sh} and Q_{lh} are dependent on sea surface temperature, which provides an efficient

damping mechanism on existing SSTA (Frankignoul and Kestenare 2002; Stephens et al. 2012). This damping mechanism (α in Eq. 7) is quantified based on the algorithm initially developed by Frankignoul et al. (1998) and recently updated by Li et al. (2020). In addition, a heat flux anomaly independent of the existing SSTA is defined as Q'_{atmo} and calculated as the residual of Q'_{net} from $-\alpha T'_1$ ("Appendix"). It is worth emphasizing that Q'_{atmo}, rather than Q'_{net}, isolates the impact of atmospheric forcing on SSTA because Q'_{net} includes the effect of damping, which is dependent on SSTA. Thus, a derivation of SSTA variability from Q'_{net} would not adequately quantify the impact of atmospheric forcing.

The storminess is represented by eddy kinetic energy (EKE) of surface wind (Feser et al. 2015) to account for the cumulative effects of storms (frequency and intensity) on SSTA. $EKE = \frac{1}{2}\left(u'^2 + v'^2\right)$ is calculated using 6-hourly horizontal wind speeds from the 20CR (1900–2012) and NCEP/NCAR reanalysis (1948–2017). The 6-hourly wind is band-pass filtered using a Lanczos filter (Duchon et al. 1979) with 49 weights to emphasize the 2-to-6-day winds and thus quantify wind energy associated with storms (Blackmon et al. 1977; Schemm and Schneider 2018).

3 Results

3.1 Changes in atmospheric forcing in the past century

Atmospheric circulation over the subpolar North Atlantic has significantly changed over the past century, as evidenced by a poleward shift of the storm track and an increase in storminess (e.g., Feser et al. 2015; Ulbrich et al. 2009; Wang et al. 2013). According to the combination of 20CR and NCEP/NCAR reanalysis dataset, surface wind eddy kinetic energy (EKE) has significantly increased northward of 45° N, where the climatological jet stream and storm track are located (Fig. 6e and f). Averaged over the cold blob (Fig. 1a), the annual mean EKE has been increasing at a rate of 1.5 m^2 s^{-2} century^{-1} (Fig. 6e), and the EKE increase in the convection season has been 2.0 m^2 s^{-2} century^{-1} (Fig. 6f). This increased EKE might have some association with a freshening subpolar North Atlantic, suggesting an implicit role of salinity (Oltmanns et al. 2020). While addressing the causes of EKE trends is beyond the scope of this study, the increased surface wind EKE is expected to perturb the ocean surface and induce greater heat loss from the ocean to the atmosphere. By linearly regressing $-Q'_{atmo}$ (the minus sign reverses the direction of the heat flux, and the positive value of $-Q'_{atmo}$ indicates that the ocean is losing more heat to the atmosphere) upon the local EKE, we find that a 1 m^2 s^{-2} increase in EKE corresponds to a 3 to

a ERSST

b HadISST

c Kaplan

-1 -0.8 -0.6 -0.4 -0.2 -0.1 0 0.1 0.2 0.4 0.6 0.8 1
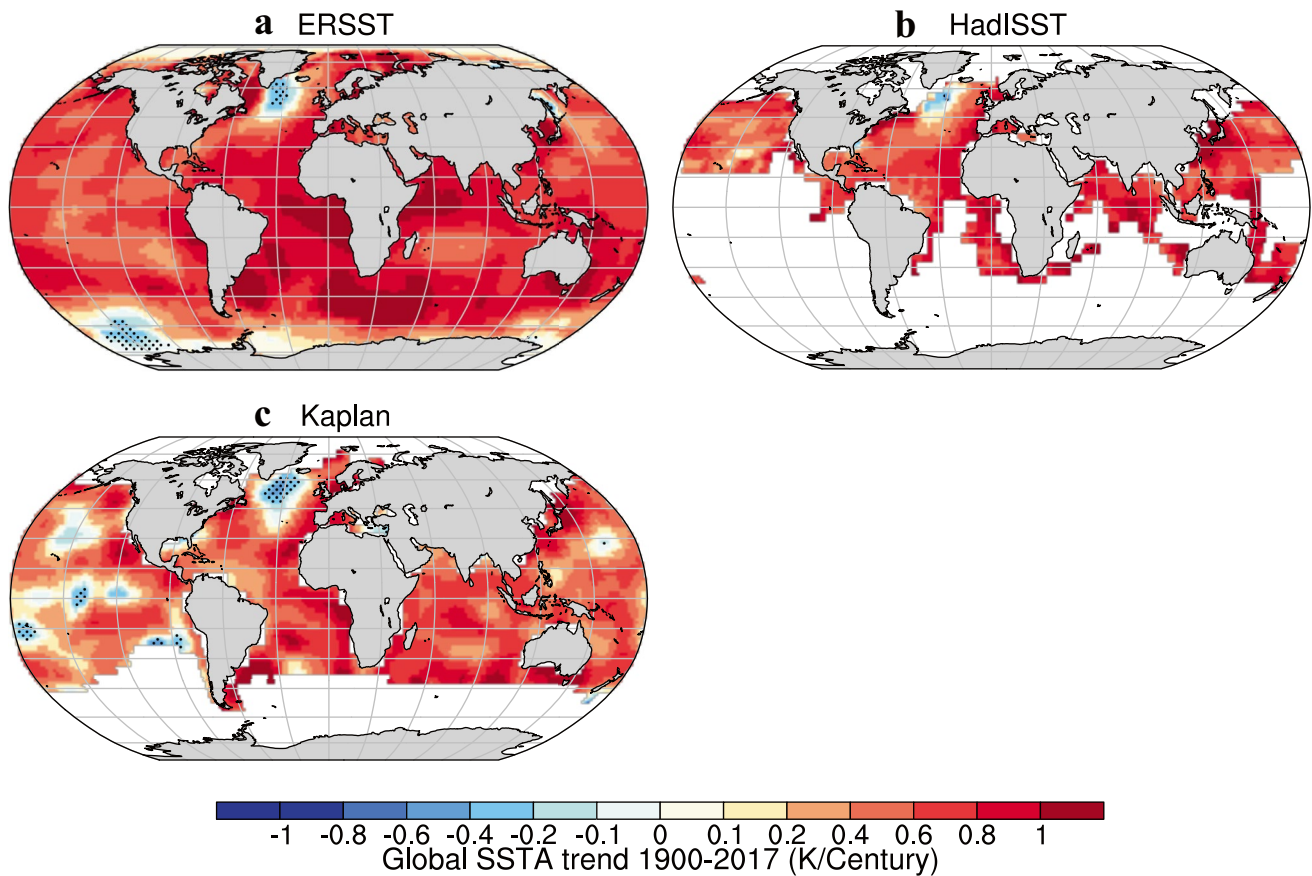Global SSTA trend 1900-2017 (K/Century)

Fig. 4 Global SSTA trend (K Century^{-1}) in three SST datasets: **a** ERSST; **b** HadISST; and **c** Kaplan. The trends are calculated using linear regression method (shaded). The stippled grid cells are where SSTA cooling trend is significant at 0.05 level. For each dataset, grid cells with more than half of the records missing are excluded when calculating linear trend
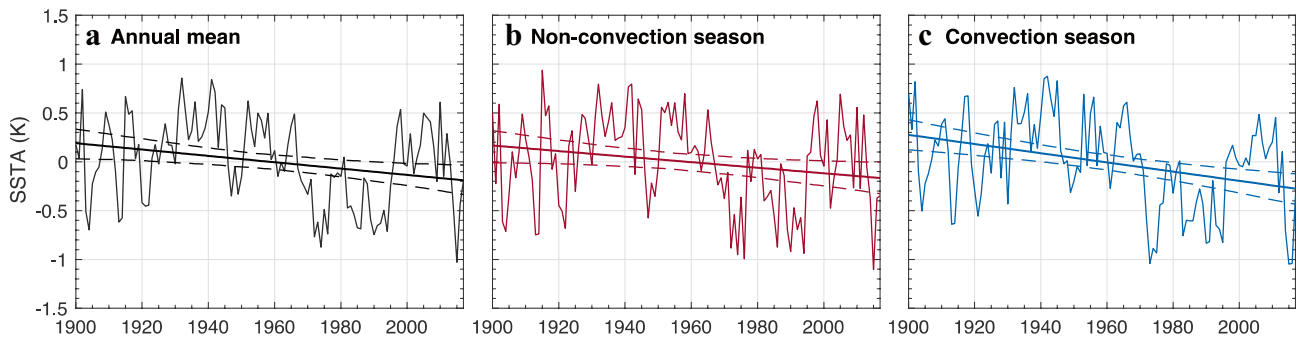
a Annual mean

b Non-convection season

c Convection season

Fig. 5 Observed SSTA time series (1900–2017) over the cold blob region: **a** Annual mean; **b** average over the non-convection season, and **c** average over the convection season. The thick lines are the lin-ear trend of the SSTA, and the thin dashed lines are the 95% uncertainty range of the trend lines

4 W m^{-2} increase in oceanic heat loss to the atmosphere (Fig. 6c, d) over the subpolar North Atlantic, i.e., a cooling effect on SSTA. The increased cooling induced by storminess decreases the SST, as shown by the EKE regressed upon the cold blob index (Fig. 6a, b).

There are potentially large uncertainties in the EKE estimation with the 20CR reanalysis data prior to the 1950s (e.g., Chang and Yan 2016), but we have repeated the EKE and $-Q'_{atmo}$ analysis for the 1950–2017 period only and found that the relationship obtained in Fig. 6c, d still holds (not shown). Thus, even with the uncertainties in EKE and

Q'_{atmo} in the earlier records, the two variables consistently imply a role for the atmosphere in cooling the subpolar North Atlantic over the past century.

Our results are consistent with previous studies suggesting the role of the atmosphere, especially jet streams, in forcing air-sea heat flux and SSTA variability in the extratropical ocean (Kushnir et al. 2002; Ma et al. 2020). Thus, the above regression analysis suggests that the observed increase in storminess is expected to contribute to the formation of a cold blob through both direct and indirect effects, as we will show next.

3.2 Direct and indirect effects of local atmospheric forcing in the cold blob region

The impact of atmospheric forcing on SSTA is quantified as the net surface heat flux anomaly due to changes in atmospheric variables (Q'_{atmo}), i.e., air temperature, surface humidity, and surface wind (see "Appendix" and Li et al. 2020). Using the combined 20CR, NNR, and ERA5, Q'_{atmo} averaged over the cold blob, yields a negative trend over the past century (-10.4 W m^{-2} century^{-1}; Fig. 3a), indicating that the atmosphere has induced more heat loss from the ocean (Fig. 7a). We do not further decompose the Q'_{atmo} trend into the portion caused by greenhouse gases or anthropogenic aerosols (Chemke et al. 2020), as the focus here is on the net effect of the Q'_{atmo} change on the SSTA trend. This increased heat loss, which provides a *direct* cooling mechanism for the sea surface, is stronger during the cold season (December-January–February-March, i.e., convection season; -14.2 W m^{-2} century^{-1}) than during the warm season (July–August–September–October, i.e., non-convection season; -4.5 W m^{-2} century^{-1}) (Figs. 3b, c and 7a). The estimated linear trend in Q'_{atmo} varies by ~ 18% with the choice of reanalysis products. Specifically, with the 20CR and NNR combined average, the trend in annual mean Q'_{atmo} is -10.6 W m^{-2} century^{-1}; but it is -8.8 W m^{-2} century^{-1} with the 20CR and ERA5 combination (Fig. 3d and g). However, the reanalysis products consistently yield a net cooling effect of the atmosphere on SST in the cold blob region. Furthermore, all three combinations suggest a notably stronger cooling effect during the convection season compared to the non-convection season (Fig. 3e and h versus Fig. 3f and i).

With the atmosphere drawing more heat loss from the ocean surface during the cold (convection) season, the frequency of convection will increase, as shown by an empirical relationship (Eq. 11) between convection and the turbulent heat flux[6] derived from the PWP mixed layer model.

According to this relationship, convection frequency over the cold blob depends nonlinearly on the magnitude of the turbulent heat flux. Convection frequency is more sensitive to a heat flux increase when the base turbulent heat flux value is low compared to when the base turbulent heat flux value is high (Fig. 7b). In other words, as the turbulent heat flux over an area increases, the likelihood of convection increases, but the rate of that increase slows as the fluxes get larger. From the 1900–2017 climatology of surface turbulent heat fluxes, the probability of wintertime convection over the cold blob region is calculated to be 78% and a 1 W/m^2 increase in surface heat flux is expected to increase that frequency by 0.6% (Fig. 7b). Since convection mixes cold subsurface water into the surface ocean, the atmospheric forcing also provides an *indirect* cooling mechanism for wintertime SSTA in the cold blob region.

3.3 Simulation of SSTs in the cold blob region using an idealized 1-D heat balance model

The *direct* (heat flux anomaly) and *indirect* (heat flux-induced convection) effects of atmospheric forcing on the cold blob are quantified using the idealized one-dimensional, two-compartment heat balance model formulated in Eqs. 9–10. In the model, SST variability is directly forced by the air-sea heat flux and is affected by heat exchange with the subsurface layer. We perform four simulations with the *direct* and *indirect* processes added sequentially into the idealized model. The assumptions and formulations of the four simulations are summarized in Table 1.

3.3.1 Atmospheric white noise as the only forcing

In the first simulation, the only forcing on SSTA is atmospheric white noise (term 1 in Eq. 9), which is approximated as a zero-centered normal distribution function. Thus, the two-compartment model is simplified as a Hasselmann model (Hasselmann 1976). As expected, the SSTA trend averaged over 1000 runs of this simulation is 0.0 K century^{-1}. However, there is a large uncertainty in the trend, with a 95% confidence interval of $[-0.34, 0.34]$ K century^{-1} (Fig. 8). Comparing this simulation with observations, the probability for atmospheric white noise alone to generate an observed SSTA cooling trend is 18.4% if the model parameters are derived from a combination of 20CR, NNR and ERA5 (Fig. 8). The combination of 20CR and NNR (20CR and ERA5) renders a probability of 16.5% (12.6%) (Fig. 8). This non-negligible probability for atmospheric white noise to generate a long-term SSTA cooling trend reflects the large heat inertia of the subpolar ocean (Buckley et al. 2019). Essentially, the ocean integrates atmospheric forcing, thereby preserving low-frequency SSTA variability (Hasselmann 1976; Chen et al. 2016; Cane et al. 2017).

---

[6] During the convection (cold) season, a heat flux anomaly results mainly from the turbulent heat flux (Frankignoul and Kestenare 2002). Thus, the empirical relationship is between the turbulent heat flux and the probability of convection.

Fig. 6 Annual mean (**a**) and convection-season (DJFM) (**b**) eddy kinetic energy (EKE) of surface wind regressed on the cold blob index (shaded, units: m² s⁻² K⁻¹), with the index defined as -SSTA over the grid cells stippled in Fig. 1a). **c, d** Are local atmospheric cooling rate (−Q'_{atmo}; the minus sign indicates that the atmospheric component of the heat flux exerts a cooling effect on local SST) regressed on local EKE (shaded, units: W m⁻²/ [m² s⁻²]) for annual mean (**c**) and the convection season (**d**). **e** and **f** Are, respectively, the 1900–2017 trend in annual mean (**e**) and convection-season (**f**) surface wind EKE (units: m² s⁻² century⁻¹). In each plot, the stippled grid cells are where the regression coefficients (**a–d**) or linear trends (**e, f**) are statistically significant at $\alpha = 0.05$ level based on student-t test
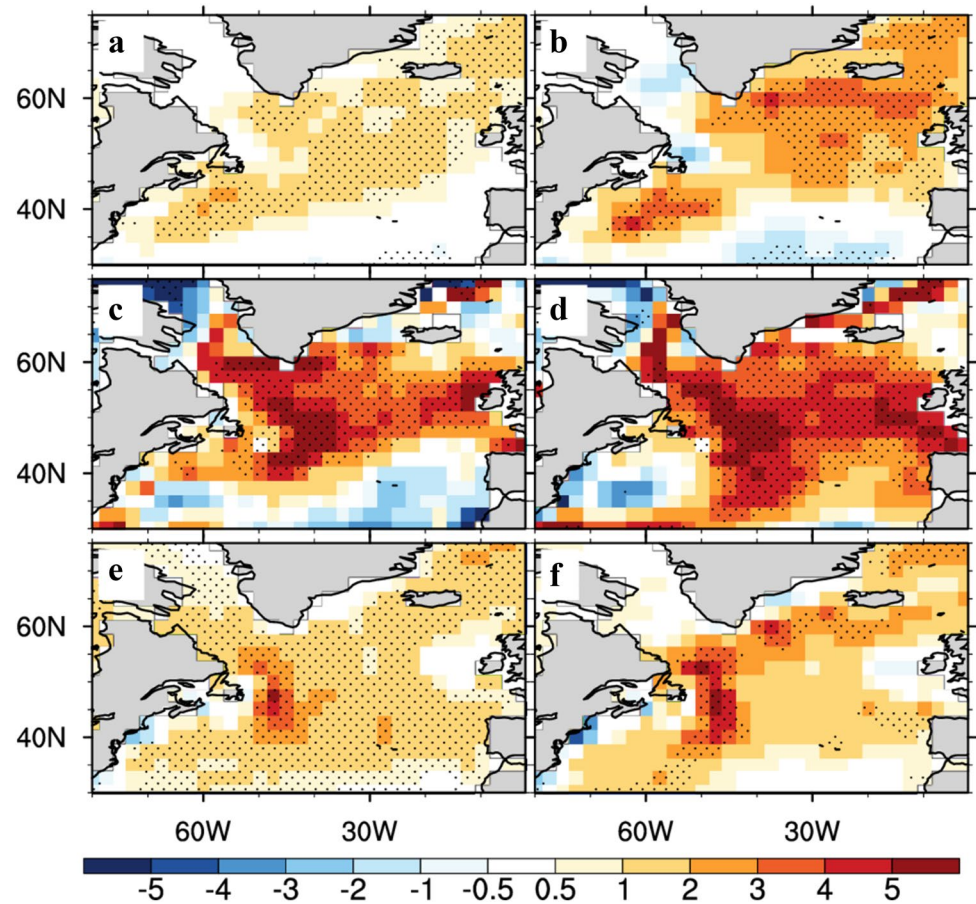
3.3.2 Adding the trend in atmospheric forcing

The observed trend in atmospheric forcing (Fig. 7a; term 2 in Eq. 9) is now added to the white noise in the second simulation (Fig. 9a). With an imposed trend of − 10.40 W m⁻² century⁻¹ in Q'_{atmo}, the model simulations yield a − 0.21 (± 0.30) K century⁻¹ trend in the annual mean SSTA. Compared to observations (− 0.39 K century⁻¹), this *direct* atmospheric forcing explains 54% (± 77%) of the SSTA trend in the cold blob region (gray bars in Fig. 9a). With the uncertainties in the Q'_{atmo} trend due to the use of different reanalysis products, the resultant SSTA trends differ. Using the Q'_{atmo} trend derived from the combination of 20CR and NNR, the simulated SSTA trend is − 0.22 (± 0.32) K century⁻¹ (blue bars in Fig. 9a), while Q'_{atmo} trend from the combination of 20CR and ERA produces an SSTA trend of − 0.16 (± 0.27) K century⁻¹ (red bars in Fig. 9a). Overall, the simulated SSTA trend and the corresponding uncertainty range are qualitatively consistent. Thus, in the following text, we discuss only the SSTA trend produced by the simulations with model parameters derived from the combination of 20CR, NNR and ERA5 (gray bars in Fig. 9). The results from the other two combinations are shown in the related figures.

This SSTA trend, however, does not significantly differ between the cold season (convection season) and warm season (non-convection season). Specifically, the SSTA trend for the convection season is − 0.22 (± 0.31) K century⁻¹, while it is − 0.21 (± 0.30) K century⁻¹ for the non-convection season. Considering the uncertainty range, the seasonal difference in the atmosphere-forced SSTA trend is insignificant (gray bars in Fig. 9a). This insignificance in the simulated trends is attributed to the dependence of SSTA on initial conditions. Considering the long memory of convection-season SSTAs, there is insufficient time for wintertime cooling effects to be damped prior to the following summer. Thus, the cold winter SSTAs serve as initial conditions for the non-convection season SSTAs thereby contributing to a cooling trend for the non-convection season SSTA and smoothing out seasonal differences in the SSTA trend that would otherwise be expected.
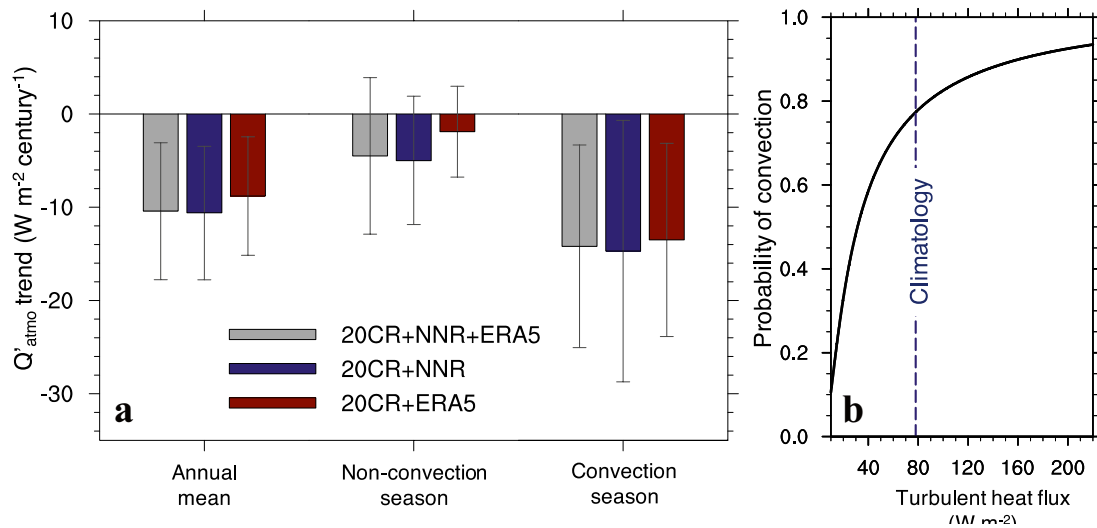
Fig. 7 **a** Trend in Q'_{atmo} over the cold blob region during 1900–2017 (W m^{-2} century^{-1}) as derived from different reanalysis products. The error bars are the 95% confidence interval of the linear trend. A negative value means that the atmosphere is exerting a stronger cooling effect on the ocean surface. **b** Empirical relationship between probability of convection (y-axis) over the cold blob region (stippled in Fig. 1a) and surface turbulent heat flux (x-axis) as derived from the PWP model simulations (Eq. 11)

3.3.3 Adding oceanic adjustment: the case with constant surface–subsurface heat exchange

The third simulation includes the surface–subsurface coupling with a fixed heat exchange rate q (term 3 in Eq. 9), which reflects the adjustment of ocean stratification to surface forcing. Specifically, as the atmospheric forcing cools the mixed layer (Fig. 9b), the temperature difference between the surface and subsurface layer decreases. This decrease in the temperature gradient renders eddy diffusivity and subsurface entrainment processes during the convection season less effective in cooling the surface temperature. At the same time, detrainment during the non-convection season becomes less effective in warming the subsurface layer. The subsequent subsurface cooling then impacts the mixed layer in the convection season, thus prolonging the surface cooling signal.

According to the simulations for this third case, the addition of surface–subsurface coupling further enhances the cooling trend forced directly by the atmosphere, with an annual mean SSTA trend of -0.27 (± 0.29) K century^{-1}; gray bar in Fig. 8b). The SSTA trend for the convection and non-convection seasons are -0.28 (± 0.30) K century^{-1} and -0.26 (± 0.29) K century^{-1}, respectively (gray bars in Fig. 9b). Thus, due to the seasonal dependence of entrainment and detrainment processes (Fig. 2a) and the competing effects of entrainment (counteracting) and detrainment (reinforcing) on atmospherically forced SSTA, the adjustment of ocean stratification reverses the seasonality of the SSTA cooling trend in the second simulations (Fig. 9a, b).

3.3.4 Adding oceanic adjustment: the case with a trend in the surface–subsurface heat exchange

As explained above, atmospheric cooling at the surface indirectly forces SSTA by inducing stronger convection which subsequently entrains subsurface water (Fig. 7b). With a negative trend in Q'_{atmo} over the past century (Fig. 7a), convection would have become more frequent in the cold blob region, meaning that the heat exchange rate between the surface and subsurface (q_1 in Eq. 1) should be nonstationary throughout the simulation.

We account for this nonstationarity in the fourth simulation. Specifically, we now account for changes in q_1 due to the surface heat flux trend during the convection season[7] (term 4 in Eq. 9). With this effect included, the model-simulated annual mean SSTA trend is now -0.36 (± 0.30) K century^{-1}, which explains 92% ($\pm 77\%$) of the observed SSTA cooling trend (gray bars in Fig. 9c). Compared to the simulation only considering *direct* atmospheric forcing (gray bars in Fig. 9a), the SSTA cooling trend is now enhanced by -0.15 K century^{-1}, a 38% increase in the SSTA trend that can be explained by the two-compartment model (Fig. 9a compared to Fig. 9c). Since the entrainment process is only present during the convection season, the SSTA trend in the convection (cold) season (-0.37 [± 0.30] K century^{-1}) is now slightly stronger than in the

---

[7] Observations show that the convection-season entrainment rate increases during 1950–2009, yet the non-convection-season detrainment does not have a significant trend (Fig. 2b, c). Thus, only the q_1 change during the convection season is considered in this study.

Table 1 Description of the simulations with the direct and indirect atmospheric forcing processes added sequentially into the idealized model

Goal of the experiments: isolate the *direct* (Q'_{atmo}) and *indirect* (thermal adjustment and entrainment) forcing exerted by the atmosphere on the cold blob

| Experiment ID		Assumptions	Model equations
Direct forcing	Exp. 1	Q'_{atmo} is the only forcing and is parameterized as a normally distributed white noise	$\rho C_p h_1 \frac{\partial T'_1}{\partial t} = -\alpha T' + N(0, \sigma^2)$
	Exp. 2	Q'_{atmo} is the only forcing on SSTA and is parameterized as a normally distributed white noise plus a seasonally dependent linear trend	$\rho C_p h_1 \frac{\partial T'_1}{\partial t} = -\alpha T' + N(0, \sigma^2) + Q'_{atmo\_trend}$
Indirect forcing	Exp. 3	Besides the atmospheric forcing terms in Exp. 2, the surface–subsurface thermal adjustment is considered. In the experiment, the heat exchange rate between the two compartments are set as seasonal climatology	Compartment 1 (Surface): $\rho C_p h_1 \frac{\partial T'_1}{\partial t} = -\alpha T' + N(0, \sigma^2) + Q'_{atmo_{trend}} + \rho C_p \bar{q}_1 (T'_2 - T'_1)$ Compartment 2 (Subsurface): $\rho C_p h_2 \frac{\partial T'_2}{\partial t} = \rho C_p \bar{q}_2 (T'_1 - T'_2)$
	Exp. 4	Same as Exp. 3, but the changes in entrainment (q'_1) in response to surface heat flux is considered. In the simulation, q'_1 is derived from the PWP model (Eq. 11)	Compartment 1 (Surface): $\rho C_p h_1 \frac{\partial T'_1}{\partial t} = -\alpha T' + N(0, \sigma^2) + Q'_{atmo_{trend}} + \rho C_p \bar{q}_1 (T'_2 - T'_1) + \rho C_p q'_1 (\overline{T_2} - \overline{T_1})$ Compartment 2 (Subsurface): $\rho C_p h_2 \frac{\partial T'_2}{\partial t} = \rho C_p \bar{q}_2 (T'_1 - T'_2)$
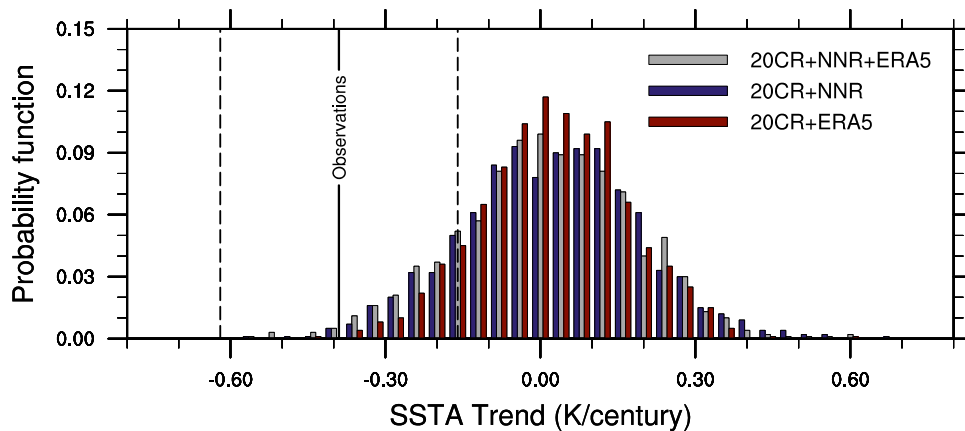
Fig. 8 Probability function of SSTA trend (K/century) forced by atmospheric white noise only (bars; term 1 in Eq. 9). The gray bars represent the SSTA trend calculated using the damping coefficients (α) and the standard deviation of atmospheric forcing (σ) from the combination of 20CR, NNR, and ERA5, while the blue (red) bars represent the SSTA trend with model parameters derived from 20CR and NNR (20CR and ERA5). The solid black line is the observed trend of the annual mean SSTA during 1900–2017. The black dashed lines are the 95% confidence intervals of the observed trend

non-convection (warm) season (-0.35 [± 0.29] K century^{-1}) (Fig. 9c). However, given the uncertainty range of the SSTA trend, the seasonal differences are not statistically significant. With this result, we surmise that ocean transport plays a role in setting the observed seasonality of the SSTA trend.

This last set of simulations demonstrates that the subsurface waters beneath the mixed layer play a significant role in generating the observed cold blob. This temporal variation of the exchange of heat between the two layers (expressed as q'_1

in Eq. 9) was neglected in previous studies, which assumed a constant surface/subsurface heat exchange rate (Gregory 2000; Held et al. 2010; Gupta and Marshall 2018). Without this *indirect* atmospheric forcing mechanism, the two-compartment model produces insufficient cooling to explain the cold blob. It is noteworthy that the entrainment rate calculated using observed mixed layer depths (MLD) is larger than that derived from the empirical probability function (Fig. 7b). Specifically, the probability curve constructed from the PWP model suggests
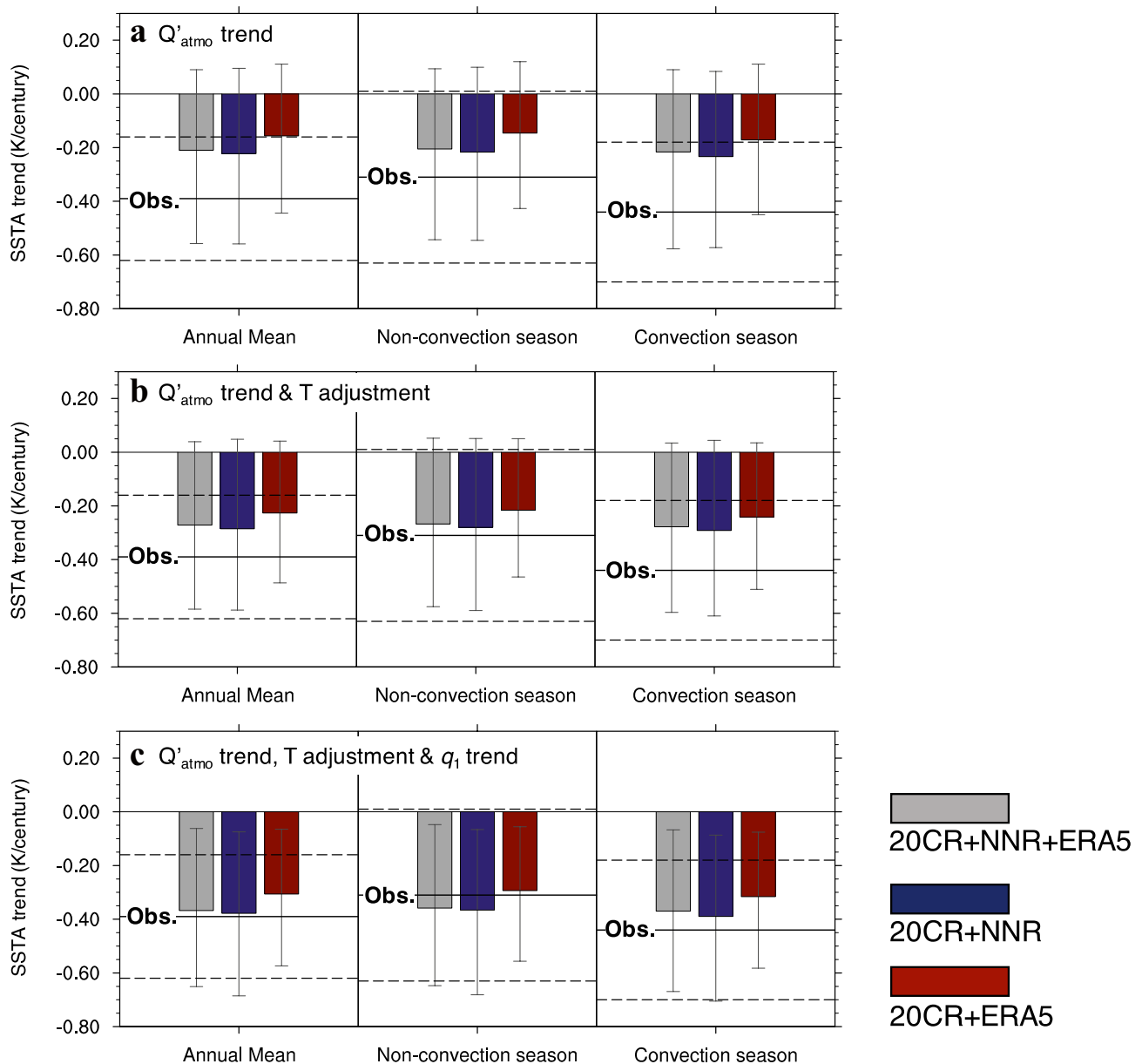
Fig. 9 Centennial SSTA trend (bars, K/century) simulated by the idealized two-compartment model with terms on the right-hand-side of Eq. (9) sequentially added: **a** simulations with the 1900–2017 trend in Q'_{atmo} added to the white noise (terms 1 and 2 in Eq. 9); **b** simulations with with temperature adjustment added (terms 1, 2 and 3 in Eq. 9); and **c** simulations with all four terms in Eq. 9. The gray, blue, and red bars represent simulations with model parameters derived from the combination of different reanalysis products. In each plot, error bars are the 95% confidence intervals of the simulated SSTA trend as derived from 1000 iterations in each simulation. The solid lines mark observed SSTA trend corresponding to different seasons, and the dashed lines are the 95% confidence interval of the observed trend

that the increased heat loss from the ocean surface would lead to an 8% increase in the probability of convection over the cold blob region; while the observations suggest a 12% increase (Fig. 2b and Eq. 3). This difference is likely explained by oceanic features and processes that impact mixing and convection, yet are not accounted for in the PWP model (e.g., fronts, eddies and local baroclinic instabilities).

4 Discussion

4.1 Spatial pattern of SSTA trend forced by local processes

The contributions of 1-D processes to the local SSTA trend over the extratropical North Atlantic are analyzed by

applying the two-compartment model to each grid cell. The climatology of the entrainment and detrainment velocity at each grid cell is calculated based on the seasonal cycle of the local MLD. Similar to the basin-averaged simulations, changes in the entrainment rate are calculated from the empirical relationship between the probability of convection and the heat flux derived using the PWP model (Eq. 11).

According to the simulations, atmospheric forcing alone (Q_{atmo_trend}) generates a cooling trend in the Irminger Sea, but a weak warming trend over the eastern portion of the Labrador Sea (Fig. 10a). With the addition of the temperature adjustment term (term 3 in Eq. 9) and the entrainment trend (term 4 in Eq. 9), the spatial gradient of the atmospherically forced SSTA trend is enhanced (Fig. 10b). Overall, the two-compartment model simulates a dipole pattern in the SSTA trend as observed, confirming our conclusions based on area-averages (Fig. 9). However, the observed warming in the western portion of the Labrador Sea is still missing in the model simulations (Fig. 10), which suggests that horizontal heat transport by the ocean is needed to recreate the observed SSTA trend pattern in the Labrador Sea (Fig. 1a). As known from observations, warm surface water is advected cyclonically around this basin via a strong boundary current. Thus, we suspect that the unequal trends (Fig. 10) on opposing sides of the Labrador basin would be mitigated by the inclusion of that advection, whereby the warmed waters on the eastern side of the basin would be advected to the western side. In addition, it may be that changes in atmospheric forcing have altered the broader ocean circulation pattern such that an increased heat flux convergence over the Labrador Sea has resulted. This effect would not be captured in our 1-D model. The precise role of oceanic heat transport in creating the observed spatial pattern of subpolar North Atlantic SSTA trend is the topic of our ongoing research.

4.2 Uncertainty in the SSTA trends and attribution of the cold blob forcing mechanisms

The analysis above suggests that changes to local atmospheric forcing provide a plausible explanation for the observed SSTA trend over the cold blob (Fig. 9) and the contrasting SSTA trends of the cold blob and the Labrador Sea (Fig. 10). However, identifying which specific local mechanism is responsible for the modeled SSTA trend is hampered by model uncertainties. For example, the uncertainty range (equivalent to the 95% confidence interval) of the SSTA trend in the white-noise experiment is $\pm$ 0.34 K century^{-1}, which means there is an 18% chance that atmospheric white noise can produce a cooling trend comparable to observations (Fig. 8). Similar uncertainty ranges are obtained in the other three experiments. In the second

experiment, where the observed cooling trend in Q'_{atmo} is added, the uncertainty range of SSTA trends extends to include cases with a positive SSTA trend, meaning that in certain runs randomly-generated internal atmospheric variability is strong enough to counteract the imposed cooling (Fig. 7). The same is true in the third experiment where a temperature adjustment is considered (Fig. 9), though here the uncertainty range slightly reduces ($\pm$ 0.29 K), as expected from the added vertical damping of atmospherically forced SSTA variability (Garuba et al. 2018; Zhang 2017). Statistically, the observed SSTA trend of the past century is but one realization from this broad set of possible realizations. While the average SSTA trend (-0.36 K century^{-1}) in the fourth experiment (with all four terms in Eq. 9) matches observations (-0.39 K century^{-1}), the uncertainty range of $\pm$ 0.3 makes the attribution nondeterministic. We conclude that our results demonstrate one possible scenario in which changing atmospheric circulation in the past century forced the observed cooling trends in the cold blob region. Importantly, our results do not exclude the possibility that oceanic processes, e.g. an AMOC slowdown (Boers 2021; Caesar et al. 2018) and salinity changes in the subpolar North Atlantic (Friedman et al. 2017), play a role in creating the observed trend, though these contributions also likely fall within the uncertainty range of SSTA trends. Moving forward, it is possible that SSS changes may have more of a direct impact on SSTA variability by inhibiting local convection (Oltmanns et al. 2020).

5 Conclusions

SST over the subpolar North Atlantic has significantly cooled since the 1900s (Fig. 1a). As opposed to greenhouse gas warming produced elsewhere, this cooling trend has sparked discussion and debate on oceanic heat uptake in a changing climate. Climate model simulations have commonly attributed this cold blob to a reduction in northward heat transport induced by an AMOC slowdown (Rahmstorf et al. 2015; Caesar et al. 2018; Gervais et al. 2018), even though the relationship between AMOC and SSTA in the subpolar North Atlantic is yet to be constrained by observations (Little et al. 2020; Fan et al. 2021).

Using a two-compartment heat balance model, this study presents evidence that local atmospheric forcing might have contributed to the formation of the cold blob. In the past century, storminess has increased in the subpolar North Atlantic due to a northward migration of the jet stream (Feser et al. 2015). The increased storminess provides more frequent and intense disturbances at the sea surface, thus promoting stronger heat loss from the ocean and inducing stronger wintertime convection (Figs. 3, 6, 7). This atmospheric forcing
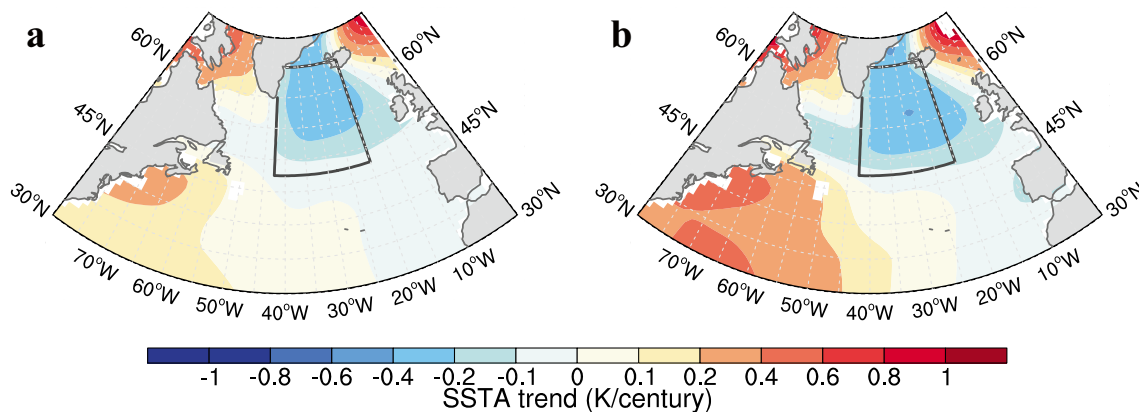
Fig. 10 100-year SSTA trend (shaded; K century^{-1}) over the extratropical North Atlantic as simulated by the idealized two-compartment heat balance model with **a** local Q'_{atmo} trend; and **b** Q'_{atmo} trend, surface–subsurface adjustment, and trends in surface–subsurface thermal coupling strength (q'_1). The black boxes delineate the geographical extent of the observed cold blob

cools SSTA *directly* and *indirectly*, collectively explaining 92% of the observed SSTA cooling trend (Fig. 9).

Although many studies have demonstrated the importance of atmospheric forcing in air-sea interaction in the extratropics (e.g., Cayan 1992; Kushnir et al. 2002; Roberts et al. 2017), the atmospheric response to SSTA and oceanic heat transport have also been recognized on multidecadal time scales (e.g., Shaffery and Sutton 2006; Gulev et al. 2013; Outten and Esau 2017). In particular, modelling studies have shown that the presence of the North Atlantic warming hole could impact the intensity and location of the mid-latitude jet stream and storm tracks in the North Atlantic (Gervais et al. 2019; Karnauskas et al. 2021), suggesting a two-way coupling between the atmosphere and ocean. As mentioned earlier, this two-way coupling is not considered in our current analysis. Future work is needed to investigate how this coupling would impact the cold blob SSTA trend and its associated uncertainty.

Cognizant of the simplifications of a 1-D heat balance model and of recent studies that have demonstrated the influence of horizontal ocean advection on SST in the subpolar North Atlantic, we stress that features not accounted for in our simple model, namely the AMOC and oceanic heat and freshwater fluxes unrelated to the AMOC, may also contribute to the observed cooling trend over the cold blob. However, our results suggest that local processes are a likely contributor, whose effects could be more important than what previous modeling studies have indicated (e.g., Keil et al. 2020; Rahmstorf et al. 2015). In addition, we hypothesize that the large spread in climate model simulations of the cold blob is due to model differences in the variable jet stream location and strength (Barnes and Polvani 2013) and jet-related atmospheric eddies (Iqbal et al. 2018). This hypothesis is to be tested in our ongoing study.

Appendix: Decomposition of Q'_{net}

Air-sea heat flux anomaly ($Q'_{net} = Q'_{SW} - Q'_{LW} - Q'_{SH} - Q'_{LH}$) is a forcing mechanism on SSTA. However, due to its dependence on SSTA, it is also a damping mechanism (Stephens et al. 2012). For example, positive SSTA increases air-sea temperature and humidity differences, which induces a stronger sensible and latent heat flux from ocean to the atmosphere and thus restores the existing SSTA (i.e., a damping mechanism). The damping and forcing mechanism exerted by Q'_{net} can be quantified as:

$$Q'_{net} = -\alpha T' + Q'_{atmo}. \tag{A1}$$

On the right-hand side of Eq. (A1), the term $-\alpha T'$ quantifies the damping mechanisms which represents the dependence of Q'_{net} on existing SSTA. The other term Q'_{atmo} quantifies the forcing mechanism which is the anomalies in heat flux purely due to changes in atmospheric variables.

The decomposition presented in Eq. (A1) has been formulated by Li et al. (2020) based on bulk formula that relate the turbulent heat fluxes to surface wind speed ($|U|$), the air-sea temperature difference ($T - T_a$), and the air-sea humidity difference ($q - q_a$) as:

$$Q_{SH} = \rho_a C_D |U| C_p^a (T - T_a), \tag{A2}$$

$$Q_{LH} = \rho_a C_D |U| L_v (q - q_a). \tag{A3}$$

In Eqs. (A2) and (A3), $\rho_a = 1.225 \text{ kg m}^{-3}$ is the density of air, $C_D = 1.15 \times 10^{-3}$ is the transfer coefficient for sensible and latent heat, $C_p^a = 1004 \text{ J Kg}^{-1} \text{ K}^{-1}$ is the specific heat of air, and $L_v = 2.5 \times 10^6 \text{ J Kg}^{-1}$ is the latent heat of vaporization. According to the Reynold's decomposition ($|U| = \overline{|U|} + |U|'; T - T_a = (\overline{T} - \overline{T}_a) + (T' - T'_a)$,

$q - q_a = \left(\overline{q} - \overline{q}_a\right) + \left(q' - q'_a\right)$; where overbars are monthly climatology and primes are the deviation from climatology) and neglecting the second order terms, the turbulent heat flux anomalies can be quantified as:

$$Q'_{SH} = \rho_a C_D C_p^a \left\{ |\overline{U}| \left(T' - T'_a\right) + |U|'\left(\overline{T} - \overline{T}_a\right) \right\}, \quad (A4)$$

$$Q'_{LH} = \rho_a C_D L_v \left\{ |\overline{U}| \left(q' - q'_a\right) + |U|'\left(\overline{q} - \overline{q}_a\right) \right\}. \quad (A5)$$

As the atmosphere near the ocean surface is saturated, and the saturation humidity is a function of temperature, q' is determined solely by T' and is formulated as $q' = \frac{\partial q}{\partial T}\big|_{\overline{T}} T'$. Plug in the temperature dependence of q', Eq. (A5) can be expressed as:

$$Q'_{LH} = \rho_a C_D L_v \left\{ |\overline{U}| \left(\frac{\partial q}{\partial T}\Big|_{\overline{T}} T' - q'_a\right) + |U|'\left(\overline{q} - \overline{q}_a\right) \right\}. \quad (A6)$$

Equations (A4) and (A6) demonstrate that anomalies in sensible and latent heat fluxes are a function of SSTA (T') and atmospheric variables. Anomalies in the atmospheric variables ($|U|'$, T'_a and q'_a) may result from internal atmospheric variability or be the response to the underlying SSTA. To quantify the response of the atmospheric variables to SSTA, we further separate the anomalies in atmospheric variables into two components: anomalies due to SSTA (we assume a linear relationship) and a residual that is due to the atmospheric internal variability. With this separation, Eqs. (A4) and (A6) are expressed as:

The dependence of turbulent heat flux on SSTA (term in brackets on the right-hand side of Eq. 10) provides an important SSTA damping mechanism, whose intensity can be quantified by a damping coefficient, α. As shown in Eq. (A9), $\alpha = \alpha_{self} + \alpha_{|U|} + \alpha_{thermal}$, consists of three components: a direct response of sensible and latent heat flux to SSTA (α_{self}), the response of wind speed to SSTA ($\alpha_{|U|}$), and the thermal adjustment of air temperature and humidity to SSTA ($\alpha_{thermal}$). The term $\alpha_{self} = \rho_a C_D \overline{|U|}\left(C_p^a + L_v \frac{\partial q}{\partial T}\big|_{\overline{T}}\right)$ is determined by the background wind speed ($\overline{|U|}$) and the sensitivity of saturation specific humidity to SSTA, which increases exponentially with background SST according to the Clausius–Clapeyron Equation. The terms $\alpha_{|U|} = \rho_a C_D \left[C_p^a\left(\overline{T} - \overline{T}_a\right) + L_v\left(\overline{q} - \overline{q}_a\right)\right]\frac{\partial |U|}{\partial T}$ and $\alpha_{thermal} = -\rho_a C_D \overline{|U|}\left(C_p^a \frac{\partial T_a}{\partial T} + L_v \frac{\partial q_a}{\partial T}\right)$ depend on the partial derivatives of $|U|'$, T'_a, and q'_a with respect to SSTA, which can be calculated based on the covariance between SSTA and $|U|'$, T'_a, and q'_a when the SSTA leads by one month, similar to Frankignoul et al. (1998), i.e.,

$$\frac{\partial |U|}{\partial T} = \frac{cov\left(|U|', T'(-1)\right)}{var(T'(-1))} \quad (A10)$$

$$\frac{\partial T_a}{\partial T} = \frac{cov\left(T'_a, T'(-1)\right)}{var(T'(-1))} \quad (A11)$$

$$Q'_{SH} = \rho_a C_D C_p^a \left\{ |\overline{U}| \left(T' - \frac{\partial T_a}{\partial T} T'\right) + \frac{\partial |U|}{\partial T} T'\left(\overline{T} - \overline{T}_a\right) \right\} + Q'_{SH\_res}, \quad (A7)$$

$$Q'_{LH} = \rho_a C_D L_v \left\{ |\overline{U}| \left(\frac{\partial q}{\partial T}\Big|_{\overline{T}} T' - \frac{\partial q_a}{\partial T} T'\right) + \frac{\partial |U|}{\partial T} T'\left(\overline{q} - \overline{q}_a\right) \right\} + Q'_{LH\_res}. \quad (A8)$$

In Eqs. A7 and A8, Q'_{SH_res} and Q'_{LH_res} are the residuals of the sensible heat flux and latent heat flux, respectively. Adding Eqs. A7 and A8, the turbulent heat flux anomalies are quantified as:

$$\frac{\partial q_a}{\partial T} = \frac{cov\left(q'_a, T'(-1)\right)}{var(T'(-1))} \quad (A12)$$

$$Q'_{SH} + Q'_{LH}$$

$$= \left\{ \underbrace{\rho_a C_D |\overline{U}| \left(C_p^a + L_v \frac{\partial q}{\partial T}\Big|_{\overline{T}}\right)}_{\alpha_{self}} + \underbrace{\rho_a C_D \left[C_p^a\left(\overline{T} - \overline{T}_a\right) + L_v\left(\overline{q} - \overline{q}_a\right)\right]\frac{\partial |U|}{\partial T}}_{\alpha_{|U|}} - \underbrace{\rho_a C_D |\overline{U}| \left(C_p^a \frac{\partial T_a}{\partial T} + L_v \frac{\partial q_a}{\partial T}\right)}_{\alpha_{thermal}} \right\} T' + Q'_{SH\_res} + Q'_{LH\_res}. \quad (A9)$$

With the quantification of α, the turbulent heat flux anomalies (Eq. A9) can be partitioned as:

$$-Q'_{SH} - Q'_{LH} = -\alpha T' + Q'_{res}. \qquad (A13)$$

The term $Q'_{res} = -Q'_{SH\_res} - Q'_{LH\_res}$ is the residual of turbulent heat flux anomalies from the damping mechanism, which is independent of SSTA and represents turbulent heat flux anomalies due to atmospheric variability. In addition, we assume that the radiative heat flux ($Q'_{SW} - Q'_{LW}$) is mainly determined by the atmosphere (Frankignoul and Kestenare 2002). Collecting terms, we quantify $Q'_{atmo} = Q'_{sw} - Q'_{lw} + Q'_{res}$ as the atmospheric contribution to the net surface heat flux anomaly.

Declarations

Conflict of interest The authors declare that they have no conflict of interest.

References

Alexander MA, Deser C (1995) A mechanism for the recurrence of wintertime mid-latitude SST anomalies. J Phys Oceanogr 25:122–137

Alexander MA, Scott JD, Deser C (2000) Processes that influence sea surface temperature and ocean mixed layer depth variability in a coupled model. J Geophys Res 105:16823–16842

Barnes EA, Polvani L (2013) Response of Midlatitude jets, and of their variability to increased greenhouse gases in the CMIP5 models. J Climate 26:7117–7135

Blackmon ML, Wallace JM, Lau N-C, Mullen SL (1977) An observational study of the Northern Hemisphere wintertime circulation. J Atmo Sci 34:1040–1053

Boers N (2021) Observation-based early-warning signals for a collapse of the Atlantic Meridional Overturning Circulation. Nat Clim Chang 11:680–688

Buckley MW, Marshall J (2016) Observations, inferences, and mechanisms of the Atlantic Meridional Overturning Circulation: a review. Rev Geophys 54:5–63

Buckley MW, DelSole T, Lozier MS, Li L (2019) Predictability of North Atlantic sea surface temperature and upper-ocean heat content. J Clim 32:3005–3023

Caesar L, Rahmstorf S, Robinson A, Feulner G, Saba V (2018) Observed fingerprint of a weakening Atlantic Ocean overturning circulation. Nature 556:191–196

Cane MA, Clement AC, Murphy LN, Bellomo K (2017) Low-pass filtering, heat flux, and Atlantic multidecadal variability. J Clim 30:7529–7553

Carton JA, Grodsky SA, Liu H (2008) Variability of the oceanic mixed layer, 1960–2004. J Clim 21:1029–1047

Cayan DR (1992) Latent and sensible heat flux anomalies over the Northern Oceans: Driving the sea surface temperature. J Phys Oceanogr 22:859–881

Chang EKM, Yan AMW (2016) Northern Hemisphere winter storm track trends since 1959 derived from multiple reanalysis datasets. Clim Dyn 47:1435–1454

Chemke R, Zanna L, Polvani LM (2020) Identifying a human signal in the North Atlantic warming hole. Nat Commun 11:1540

Chen H, Schneider EK, Wu Z (2016) Mechanisms of internally generated decadal-to-multidecadal variability of SST in the Atlantic Ocean in a coupled GCM. Clim Dyn 46:1517–1546

Clement A, Bellomo K, Murphy LN, Cane MA, Mauritsen T, Rädel G, Stevens B (2015) The Atlantic Multidecadal Oscillation without a role for ocean circulation. Science 350:320–324

Compo GP, Whitaker JS, Sardeshmukh PD, Matsui N, Allan RJ, Yin X (2011) The twentieth century reanalysis project. Q J R Meteorol Soc 137:1–28

de Jong MF, de Steur L (2016) Strong winter cooling over the Irminger Sea in winter 2014–2015, exceptional deep convection, and the emergence of anomalously low SST. Geophys Res Lett 43:7106–7113

de Boyer MC, Madec G, Fischer AS, Lazar A, Iudicone D (2004) mixed layer depth over the global ocean: an examination of profile data and profile-based climatology. J Geophys Res 109:C12003

Deser C, Alexander MA, Timlin MS (2003) Understanding the persistence of sea surface temperature anomalies in midlatitudes. J Clim 16:57–72

Di Lorenzo E, Ohman MD (2013) A double-integration hypothesis to explain ocean ecosystem response to climate forcing. Proc Natl Acad Sci 110:2496–2499

Drijfhout S, van Oldenbourgh GJ, Cimatoribus A (2012) Is a decline of AMOC causing the warming hole above the North Atlantic in observed and modelled warming patterns? J Clim 25:8373–8379

Duchon CE (1979) Lanczos filtering in one and two dimensions. J Appl Meteorol 18:1016–1022

Fan Y, Lu J, Li L (2021) Mechanism of the centennial subpolar North Atlantic cooling trend in the FGOALS-g2 historical simulation. J Geophys Res Oceans 126:e2021JC017511

Feldstein S (2000) The timescale, power spectra, and climate noise properties of teleconnection patterns. J Climate 13:4430–4440

Feser F, Barcikowska M, Krueger O, Schenk F, Weisse R, Xia L (2015) Storminess over the North Atlantic and northwestern Europe—a review. Q J R Meteorol Soc 141:350–382

Foukal NP, Lozier MS (2018) Examining the origins of ocean heat content variability in the eastern North Atlantic subpolar gyre. Geophys Res Lett 45:11275–11283

Frankignoul C, Kestenare E (2002) The surface heat flux feedback. Part I: estimates from observations in the Atlantic and the North Pacific. Clim Dyn 19:633–647

Frankignoul C, Czaja A, L'Heveder B (1998) Air-sea feedback in the North Atlantic and surface boundary conditions for ocean models. J Climate 11:2310–2324

Friedman AR, Reverdin G, Khodri M, Gastineau G (2017) A new record of Atlantic sea surface salinity from 1896 to 2013 reveals the signatures of climate variability and long-term trends. Geophys Res Lett 44:1866–1876

Fröb F, Olsen A, Våge K, Moore GWK, Yashayaev I, Jeansson E, Rajasakaren B (2016) Irminger Sea deep convection injects oxygen and anthropogenic carbon to the ocean interior. Nat Commun 7:13244

Fu Y, Li F, Karstensen J, Wang C (2020) A stable Atlantic Meridional Overturning Circulation in a changing North Atlantic Ocean since the 1990s. Sci Adv 6:eabc7836

Garuba OA, Lu J, Singh HA, Liu K, Rasch P (2018) On the relative roles of the atmosphere and ocean in the Atlantic multidecadal variability. Geophys Res Lett 45:9186–9196

Gervais M, Shaman J, Kushnir Y (2018) Mechanisms governing the development of the North Atlantic warming hole in the CESM-LE future climate simulations. J Climate 31:5927–5946

Gervais M, Shaman J, Kushnir Y (2019) Impacts of the North Atlantic warming hole in future climate projections: mean atmospheric circulation and the North Atlantic jet. J Climate 32:2673–2689

Good SA, Martin MJ, Rayner RN (2013) EN4: Quality controlled ocean temperature and salinity profiles and monthly objective analyses with uncertainty estimates. J Geophys Res Oceans 118:6704–6716

Gregory JM (2000) Vertical heat transports in the ocean and their effect on time-dependent climate change. Clim Dyn 16:501–515

Gulev SK, Latif M, Keenlyside N, Park W, Koltermann KP (2013) North Atlantic Ocean control on surface heat flux on multidecadal timescales. Nature 499:464–467

Gupta M, Marshall J (2018) The climate response to multiple volcanic eruptions mediated by ocean heat uptake: Damping processes and accumulation potential. J Clim 31:8669–8687

Hanawa K, Sugimoto S (2004) 'Reemergence' area of winter sea surface temperature anomalies in the world's oceans. Geophys Res Lett 31:L10303

Hansen J, Nazarenko L, Ruedy R et al (2005) Earth's energy imbalance: Confirmation and implications. Science 308:1431–1435

Hasselmann K (1976) Stochastic climate models. Part I. Theory. Tellus 28:473–485

Hausmann U, Czaja A, Marshall J (2017) Mechanisms controlling the SST air-sea heat flux feedback and its dependence on spatial scale. Clim Dyn 48:1297–1307

Held I, Winton M, Takahashi K, Delworth T, Zeng F, Vallis GK (2010) Probing the fast and slow components of global warming by returning abruptly to preindustrial forcing. J Clim 23:2418–2427

Hersbach H, Bell B, Berrisford P et al (2020) The ERA5 global reanalysis. Q J R Meteorol Soc 146:1999–2049

Holliday NP, Cunningham SA, Johnson C, Gary SF, Griffiths C, Read JF, Sherwin T (2015) Multidecadal variability of potential temperature, salinity, and transport in the eastern subpolar North Atlantic. J Geophys Res Oceans 120:5945–5967

Holliday NP, Bersch M, Berx B et al (2020) Ocean circulation causes the largest freshening event for 120 years in eastern subpolar North Atlantic. Nat Commun 11:585

Hu S, Fedorov AV (2020) Indian Ocean warming as a driver of the North Atlantic warming hole. Nat Commun 11:4785

Huang B, Banzon VF, Freeman E et al (2014) Extended Reconstructed Sea Surface Temperature version 4 (ERSST.v4): Part I. Upgrades and intercomparisons. J Climate 28:911–930

IPCC (2013) Climate change 2013: the physical science basis. In: Stocker TF, Qin D, Plattner G-K, Tignor M, Allen SK, Boschung J, Nauels A, Xia Y, Bex V, Midgley PM (eds) Contribution of working Group I to the fifth assessment report of the intergovernmental panel on climate change. Cambridge University Press, Cambridge, p 1535. https://doi.org/10.1017/CBO9781107415324

Iqbal W, Leung W-N, Hannachi A (2018) Analysis of the variability of the North Atlantic eddy-driven jet stream in CMIP5. Clim Dyn 51:235–247

Josey SA, Hirschi JJ-M, Sinha B, Duchez A, Grist JP, Marsh R (2018) The recent Atlantic cold anomaly: causes, consequences, and related phenomena. Annu Rev Mar Sci 10:475–501

Josey SA, de Jong MF, Oltmanns M, Moore GK, Weller RA (2019) Extreme variability in Irminger sea winter heat loss revealed by ocean observatories initiative mooring and the ERA5 reanalysis. Geophys Res Lett 46:293–302

Kalnay E, Kanamitsu M, Kistler R et al (1996) The NCEP-NCAR 40-year reanalysis project. Bull Amer Meteor Soc 77:437–471

Kaplan A, Cane M, Kushnir Y, Clement A, Blumenthal M, Rajagopalan B (1998) Analysis of global sea surface temperature 1856–1991. J Geophys Res 103:18567–18589

Karnauskas KB, Zhang L, Amaya DJ (2021) The atmospheric response to North Atlantic SST Trends, 1870–2019. Geophys Res Lett 48:e2020GL090677

Keil P, Mauritsen T, Jungclaus J, Hedemann C, Olonscheck D, Ghosh R (2020) Multiple drivers of the North Atlantic warming hole. Nat Clim Chang 10:667–671

Kerr KA (2000) A North Atlantic climate pacemaker for the centuries. Science 288:1984–1985

Kushnir Y, Robinson WA, Bladé I, Hall NMJ, Peng S, Sutton R (2002) Atmospheric GCM response to extratropical SST anomalies: synthesis and evaluation. J Clim 15:2233–2256

Levitus S, Antonov JI, Wang J, Delworth TL, Dixon KW, Broccoli AJ (2001) Anthropogenic warming of Earth's climate system. Science 292:267–270

Li L, Lozier MS, Buckley MW (2020) An investigation of the ocean's role in Atlantic Multidecadal variability. J Climate 33:3019–3035

Little CM, Zhao M, Buckley MW (2020) Do surface temperature indices reflect centennial-timescale trends in Atlantic Meridional Overturning Circulation strength? Geophys Res Lett 47:e2020GL090888

Liu W, Huang B, Thorne PW et al (2014) Extended Reconstructed Sea Surface Temperature version 4 (ERSST.v4): Part II. Parametric and structural uncertainty estimations. J Clim 28:931–951

Ma L, Woollings T, Williams RG, Smith D, Dunstone N (2020) How does the winter jet stream affect surface temperature, heat flux, and sea ice in the North Atlantic? J Clim 33:3711–3730

Menary M, Wood RA (2018) An anatomy of the projected North Atlantic warming hole in CMIP5 models. Clim Dyn 50:3063–3080

Monterey GI, Levitus S (1997) Seasonal variability of mixed layer depth for the world ocean. US Department of Commerce, National Oceanic and Atmospheric Administration, National Environmental Satellite, Data, and Information Service

Oltmanns M, Karstensen J, Moore GWK, Josey SA (2020) Rapid cooling and increased storminess triggered by freshwater in the North Atlantic. Geophys Res Lett 47:e2020GL087207

Outten S, Esau I (2017) Bjerknes compensation in the Bergen Climate Model. Clim Dyn 49:2249–2260

Pickart R, Spall M, Ribergaard M, Moore GWK, Milliff R (2003) Deep convection in the Irminger Sea forced by the Greenland tip jet. Nature 424:152–156

Price JF, Weller RA, Pinkel R (1986) Diurnal cycling: Observations and models of the upper ocean response to diurnal heating, cooling and wind mixing. J Geophys Res 91:8411–8427

Rahmstorf S, Box JE, Feulner G, Mann ME, Robinson A, Rutherford S, Schaffernicht EJ (2015) Exceptional twentieth-century slowdown in Atlantic Ocean overturning circulation. Nat Clim Chang 5:475–480

Rayner NA, Parker DE, Horton EB et al (2003) Global analysis of sea surface temperature, sea ice, and night marine air temperature since the late nineteenth century. J Geophys Res 108:4407

Roberts CD, Palmer MD, Allan RP, Desbruyeres DG, Hyder P, Liu C, Smith D (2017) Surface flux and ocean heat transport convergence contributions to seasonal and interannual variations of ocean heat content. J Geophys Res Oceans 122:726–744

Schemm S, Schneider T (2018) Eddy lifetime, number, and diffusivity and the suppression of eddy kinetic energy in midwinter. J Clim 31:5649–5665

Schlesinger M-E, Ramankutty N (1994) An oscillation in the global climate system of period 65–70 years. Nature 367:723–726

Schneider N, Cornuelle BD (2005) The forcing of the Pacific Decadal Oscillation. J Clim 18:4355–4373

Sevellec F, Fedorov AV, Liu W (2017) Arctic sea-ice decline weakens the Atlantic Meridional Overturning Circulation. Nat Clim Chang 7:604–609

Sgubin G, Swingedouw D, Drijhout S, Mary Y, Bennabi A (2017) Abrupt cooling over the North Atlantic in modern climate models. Nat Commun 8:14375

Shaffery LC, Sutton RT (2006) Bjerknes compensation and the decadal variability of energy transports in a coupled climate model. J Clim 19:1167–1181

Stephens GL, Li J, Wild M et al (2012) An update on Earth's energy balance in light of the latest global observations. Nat Geosci 5:691–696

Ulbrich U, Leckebusch GC, Pinto JG (2009) Extra-tropical cyclones in the present and future climate: a review. Theor Appl Climatol 96:117–131

Våge K, Pickart RS, Moore GWK, Ribergaard MH (2008) Winter mixed layer development in the central Irminger Sea: the effect of strong, intermittent wind events. J Phys Oceanogr 38:541–565

Wang XL, Feng Y, Compo GP, Swail VR, Zwiers FW, Allan RJ, Sardeshmukh PD (2013) Trends and low frequency variability of extra-tropical cyclone activity in the ensemble of twentieth century reanalysis. Clim Dyn 40:2775–2800

Wills RCJ, Armour KC, Battisti DS, Hartmann DL (2019) Ocean-atmosphere dynamical coupling fundamental to the Atlantic Multidecadal Oscillation. J Clim 32:251–272

Woollings T, Gregory JM, Pinto JG, Reyers M, Brayshaw DJ (2012) Response of the North Atlantic storm track to climate change shaped by ocean-atmosphere coupling. Nat Geosci 5:313–317

Worthington EL, Moat BI, Smeed DA, Mecking JV, Marsh R, McCarthy GD (2021) A 30-year reconstruction of the Atlantic meridional overturning circulation shows no decline. Ocean Sci 17:285–299

Zhang R (2008) Coherent surface-subsurface fingerprint of the Atlantic meridional overturning circulation. Geophys Res Lett 35:L20705. https://doi.org/10.1029/2008GL035463

Zhang R (2017) On the persistence and coherence of subpolar sea surface temperature and salinity anomalies associated with the Atlantic Multidecadal Variability. Geophys Res Lett 44:7865–7875

Zhang R, Sutton R, Danabasoglu G, Kwon Y-O, Marsh R, Yeager SG, Amrhein DE, Little CM (2019) A review of the role of the Atlantic Meridional Overturning Circulation in Atlantic Multidecadal Variability and associated climate impacts. Rev Geophys 57:316–375